2024 IEEE/RSJ International Conference on Intelligent Robots and Systems (IROS)
October 14-18, 2024. Abu Dhabi, UAE

2mm Diameter Continuum Robot Tools for Suturing in Open Spina Bifida Repair

Arion Law[1,5], Nillan Nimal[1,5], Paul H. Kang[2,5], Radian Gondokaryono[3,5], James Drake[5], Tim Van Mieghem[4,5], and Thomas Looi[5]

***Abstract*— Open Spina Bifida (OSB) is a congenital neural tube defect where a major component of the procedure to repair the defect involves the closure of a lesion wound through suturing. For a minimally invasive approach, tools entering the uterus to access the fetus should be as thin as possible to minimize maternal risk. This work presents the design of a 3 degrees-of-freedom, 2mm diameter tool wrist with a bending range of motion from 0° to 90°. This wrist is capable of generating up to 2N of force measured from the end of the wrist and achieving a bending curvature of 107m^{-1} (9.35mm bending radius). A pseudo-rigid body kinematic model has been implemented for the control of this tool with a protocol for singularity mitigation and avoidance. Timed teleoperation studies explicitly demonstrate that the tool is able to reliably execute suturing with a fastest achieved time of under 3 minutes for a simple interrupted suturing technique.**

I. INTRODUCTION

Open Spina Bifida (OSB) is a congenital neural tube defect, where a segment of the spinal cord develops outside the back of the fetus in the form of a lesion. Successful repair of the defect involves dissection of the spinal cord from the lesion, internalizing the exposed spinal cord followed by closure of the lesion wound by suturing. Current research on this procedure focuses on pre-natal, minimally invasive approaches employing robotic instruments. It has been identified that suturing is the more challenging and time-consuming task in this repair [1]. Clinical research suggests that the size of the ports going into the uterus should be less than 3mm to reduce maternal complications [2].

A. Prior Works

In prior works, 2mm diameter tendon-driven continuum tool designs by Francis et. al. have been tested for suturing capabilities. However, it was demonstrated that these wrists on these tool designs are insufficiently strong to reliably execute suturing[3]. Another tendon-driven continuum tool design is also proposed by Vandebroek et al. [4] specifically for the OSB suturing application. However, the nominal diameter at the gripper is 3.4mm. A 2.8mm diameter, pre-curved concentric tube design has been proposed by Amanov et al. [5] for suturing in prostatectomy. However, the tools have a limited range of motion and require long insertion lengths to operate because it employs pre-curved concentric tube for actuation making it unsuitable for the small and shallow workspace within the uterus.

While these tool designs are capable of suturing, they either lack sufficient strength, are larger than the 3mm port size constraint or do not operate within the workspace constraints of the uterus.

B. Contribution

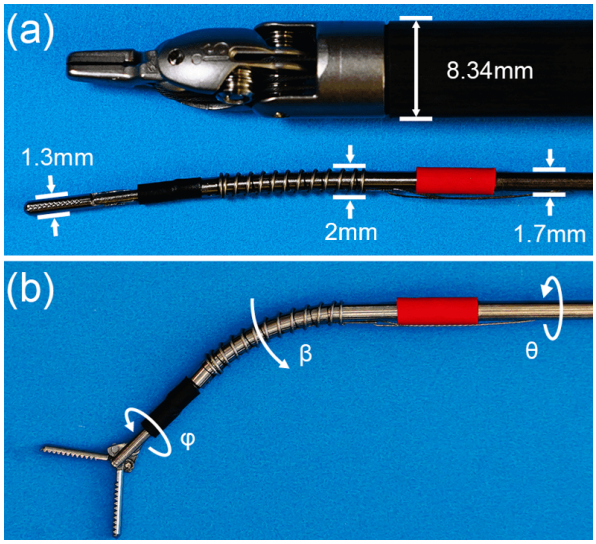

Fig. 1: a) Tool in straight wrist configuration beside a da Vinci 8mm Large Needle Driver. b) Bending configuration with labeled inner tube roll (φ), outer tube roll (θ), and outer tube bending pitch (β).

In this work, we propose a novel 2mm diameter, tendon-driven continuum wrist design seen in Fig. 1. This wrist design is significant because it has been demonstrated to exert more force at the tool tip than all other continuum wrist designs currently proposed in literature at the 2-3mm diameter scale. This is achieved while retaining the sufficient range of motion, articulation and compactness such that dexterous high force tasks are feasible with sub 3mm diameter ports.

The contributions are summarized as follows:

[1]Arion Law and Nillan Nimal are with the Department of Mechanical and Industrial Engineering, University of Toronto, Canada
[2]Paul H. Kang is with the Institute of Biomedical Engineering, University of Toronto, Canada
[3]Radian Gondokaryono is with the Department of Computer Science and the Medical Computer Vision and Robotics Lab, University of Toronto, Canada
[4]Tim Van Mieghem is with Mount Sinai Hospital, Toronto, Canada
[5]Arion Law, Nillan Nimal, Paul H. Kang, Radian Gondokaryono, James Drake and Thomas Looi are with the Wilfred and Joyce Posluns Centre for Image Guided Innovation and Therapeutic Intervention, Hospital for Sick Children, Toronto, Canada

- A 2mm diameter, tendon-driven continuum wrist capable of delivering up to 2N of force at the distal end, achieving a bending curvature of 107m^{-1} (9.35mm bending radius), while having 3 degrees-of-freedom (DoF) with 0° to 90° wrist bending range of motion.
- A kinematics solver, for this tool mounted on the dVRK Patient Side Manipulator, which is capable of navigating through the singularity configuration.
- Task timing studies of needle suturing on a suture training pad to show the feasibility of our wrist for use in OSB repair.

II. TOOL DESIGN

The tool wrist is a continuum tube design with cutouts to form compliant geometries. A wrist design with Roll-Pitch-Roll (RPR) joint sequencing was selected over other joint sequences such as Roll-Pitch-Yaw (RPY). This was done because RPR only has one orthogonal bending articulation resulting in the capability to achieve a tighter bending radius because all the compliant geometry along the length of the wrist is aligned to articulate in the same bending direction. A tighter bending radius is desirable due to the limited workspace within the uterus. The major disadvantage of a RPR wrist design is the presence of a singularity when the wrist is in a straight configuration. However, this is addressed and mitigated in the controls and kinematics of this tool.

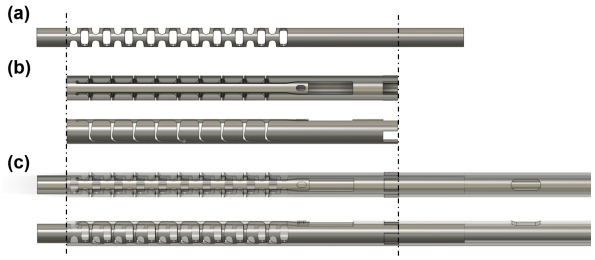

Fig. 2: Geometry visualization of the a) inner wrist tube, b) outer wrist tube (top and side view), and c) the overall assembly of both tubes (top and side view).

To achieve an RPR wrist design, two concentric tubes are employed such that the inner and outer tube can roll independently of each other. Typical concentric tube robot designs use pre-bent curvatures in the tubes to achieve bending actuation, however, this greatly limits the range of motion and the minimum achievable bending radius. Instead, tendons are employed for bending actuation to enable a large bending range. The tendon cable is attached onto the outer tube to actuate the bending of the outer tube. Due to concentric interaction, the bending curvature of the inner tube is then dictated by the curvature of the outer tube. The outer tube of the wrist is designed only to bend in one direction. Unidirectional bending is advantageous over bidirectional bending because it is possible to achieve a larger bending moment between the tendon cable and the neutral bending axis of the tube which enables greater force generation at the end of the wrist. The design of the inner tube, outer tube, and the assembly of both tubes to form the overall wrist is shown in Fig. 2. An advantage of having 2 concentrically nested tubes is that the design of the compliance patterns cut in the 2 tubes can be optimized for the expected loading cases of each tube in the wrist design. The design optimization of the 2 tubes for their specific roles allows for a stiffer and stronger overall wrist in comparison to a single tube design of comparable diameter and wall thickness where any designed pattern is a trade-off between stiffness in axial, torsional and bending loading.

A. Inner Tube Design

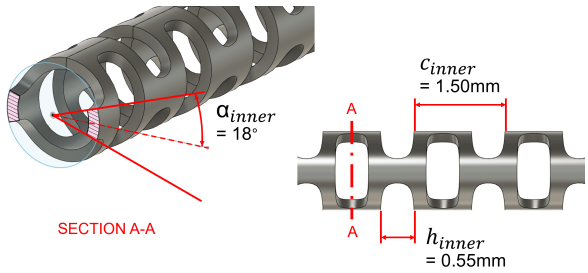

Fig. 3: Dimensions of the inner wrist tube.

The inner tube is primarily responsible for the stiffness and strength of the wrist under axial and torsional loads. The inner tube also must be compliant to the curvature set by the outer tube. Therefore, the compliant geometries on this tube are designed to be minimally stiff in bending while retaining axial and torsional stiffness. This is achieved by using symmetric, bidirectional, 2 DoF cutout geometries seen in Fig. 3. During optimization, geometries with a greater number of smaller sized cutouts in a denser pattern such as those made by Luo et al. [6] were found to reduce the bending stiffness and provide greater axial and torsional stiffness compared to the pattern presented. However, it was difficult to reliably produce tubes with cutouts smaller than 0.55mm during the fabrication of this wrist design.

B. Outer Tube Design

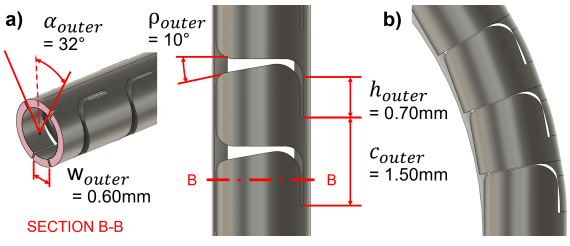

Fig. 4: a) Dimensions of the outer wrist tube and b) a simulated bending of the tube based on constant curvature beam deflection modeling.

The outer tube is responsible for setting the overall bending curvature of the wrist and is primarily responsible for the strength and stiffness of the wrist in bending. Therefore, the tube is designed to be minimally stiff during in-axis

bending (bending in the intended direction of the compliant geometries) to cooperate with actuation by the tendon cable. The outer tube also needs to be maximally stiff against lateral off-axis bending (bending that is perpendicular to the intended direction of the compliant geometries) for the purpose of exerting force during various tissue interactions. This extreme difference in stiffness between bending directions is achieved by the use of contact aided geometry seen in Fig. 4. The geometry of the compliance cutouts follow a similar design to the geometries found in Eastwood et al. [7]. The dimensions of the cutouts have been optimized so that the contact that restricts the maximum bending angle also contributes towards increasing lateral stiffness. Additionally, an articulation strip following the design of Eastwood et al. [8] is implemented along the length of this wrist (seen in Fig. 2b). Under lateral loading, this articulation strip makes contact with the other geometries and increases the overall lateral stiffness by acting as an additional bending member. A spring with an inner diameter of 1.73mm and an outer diameter of 2mm is placed over the outer tube to radially constrict the articulation strip. The tendon cable is attached to the articulation strip by looping through the hole at the end of the strip.

TABLE I: Tube cutout parameters: outer diameter (OD), inner diameter (ID), repeating sections (n), cutout spacing (c), cutout height (h), and cutout sector angle (α).

Tube	OD [mm]	ID [mm]	n [-]	c [mm]	h [mm]	α [°]
Inner	1.25	1.00	10	1.50	0.55	18
Outer	1.70	1.30	9	1.50	0.70	32

The inner and outer wrist tubes are made of Nitinol, and the inner and outer shafts leading from the wrist to the tool base are made of 304 stainless steel. The overall length of the wrist was chosen to be 15mm long. This was determined to be the shortest possible length for the inner tube to be able to bend 90° without exceeding 6% straining according to cantilevered beam deflection equations. 6% strain was taken to be the upper limit to avoid material failure and to ensure that deformation remains recoverable, staying within the elastic and superelastic region of Nitinol [9][10]. The cutout design parameters for both tubes are seen in Table I. A 4-axis laser tube cutter (RT1000 Laser Tube Cutting Machine, Preco Inc.) is used to fabricate the cutout geometries on the inner and outer tubes.

C. Tool Base Design

The actuation of the tool is achieved by integrating the shafts and cables for manipulation by daVinci Surgical System tool bases. In this way, the tool can be operated on the daVinci Research Kit (dVRK). The design of the tool base is shown in Fig. 5. The rolling actuation of the inner and outer shafts is achieved using a cable driven barrel mechanism. A winch mechanism is used to actuate the bending of the wrist by pulling on the tendon cable which runs between the inner and outer shaft. The actuation of the end-effector is achieved

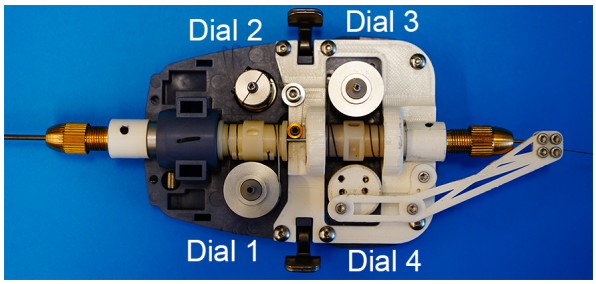

Fig. 5: Tool base design and labeled wrist articulation dial assignments: 1) outer tube roll, 2) tendon winch, 3) inner tube roll, and 4) gripper linkage mechanism.

by a planar linkage system, which moves the cable that runs inside the central lumen of the inner shaft.

D. End-Effector

The gripper mechanism from a pair of off-the-shelf laparoscopic saw-toothed grasping forceps 4Fr (1.3mm ⌀), shown in Fig. 1, is attached onto the end of the wrist for suture manipulation. The gripper mechanism is secured onto the end of the wrist using adhesive (LOCTITE®430). The grippers add an additional 14mm in length from the end of the wrist.

III. TELEOPERATION CONTROL AND KINEMATICS

A. Teleoperation Control

The dVRK Software [11] is set up to provide a Robot Operating System (ROS)-based interface for controlling the joint positions of the Patient Side Manipulator (PSM). There are a total of 7 joints, 3 joints that directly control the PSM and 4 joints that correspond to the dial positions of the tool. We employ a ROS teleoperation controller framework [12] to control our tools in Cartesian space using commands recieved from the Master Tool Manipulator (MTM). To control our tool, the controller framework requires forward kinematics (FK) and inverse kinematics (IK) solvers specific for describing our tool articulations. Our FK and IK solver for this tendon driven wrist tool is explained in the next subsection.

B. Kinematics

A pseudo-rigid body (PRB) model [13], [14] is adopted to describe the kinematic behavior of the tool. The bending of the wrist is modeled as a single pseudo-joint, allowing for the tool to be characterized using the modified Denavit-Hartenberg (DH) convention shown in Fig. 6a with parameters in Table II. As shown in Fig. 6b the kinematics for the position and orientation are decoupled, where joints q_1 to q_3 control the overall position and q_4 to q_6 control the overall orientation. The remote center of motion (RCM) for the PSM is located at frame 0 and the length from the RCM to frame 3 is $l_{RCC} = 0.4318m$. A virtual tip frame is set after frame 6 where the location determines the teleoperation controller behavior. We choose a length, l_{tip_offset} = 1.5mm to be

close to the wrist center (WRC). This is to mimic the control behaviour of the dVRK where the operator orients the tools about the wrist center when they control wrist orientation with the MTM.

The PRB model was selected for its simplicity and capabilities to produce analytical solutions, circumventing the need for numerical approximations. This is advantageous for reducing computational load and enhancing controller performance. However, a known disadvantage of discretizing the continuum wrist into rigid-body segments is the inability to consider continuum deformation resulting in inherent tip position error. This makes the solutions obtained by the PRB model less accurate than higher fidelity continuum models such as constant curvature [15], piece-wise constant strain [16], and modal shape fitting [17]. Despite this, our characterization and teleoperation testing, explained in the following sections, suggests that the tip position inaccuracy due to the lower fidelity of the PRB model is negligible.

The kinematics problem involves three parts: forward kinematics, mapping current joint states to the end-effector position and orientation; inverse kinematics, representing the reverse mapping; and singularity deviation, which ensures the tool pose is not in a singularity configuration within the workspace while also predicting and modifying the tool trajectory to navigate around the singularity.

1) Forward Kinematics: The orientation of the end-effector R_{EE} is obtained from the current joint states through the equation $R_{EE} = R_{shaft}R_{wrist}$ where R_{shaft} and R_{wrist} are shown in Fig. 6b. The rotation matrices for $R_{shaft} = R_3^0$ and $R_{wrist} = R_7^3$ are derived by propagating rotations through the DH frames. Then, the joint values q_1, q_2, q_3, the distance between the RCM and WRC l_{WRC}, tip offset l_{tip_offset} and the derived rotation matrix R_{wrist} are utilized to compute the position of the end-effector $\vec{p_{EE}}$:

$$l_{WRC} = q_3 - l_{RCC} + l_{shaft} + \frac{l_{wrist}}{2} \tag{1}$$

$$\vec{p}_{WRC} = \begin{bmatrix} x \\ y \\ z \end{bmatrix} = \begin{bmatrix} (l_{WRC})\sin(q_1)\cos(q_2) \\ (l_{WRC})\sin(q_2) \\ (l_{WRC})\cos(q_1)\cos(q_2) \end{bmatrix} \tag{2}$$

$$\vec{p}_{EE} = \vec{p}_{WRC} + \Big(l_{tip\_offset}\Big) R_{wrist} \begin{bmatrix} 0 & 0 & 1 \end{bmatrix}^T \tag{3}$$

2) Inverse Kinematics: Since orientation and position are decoupled for the kinematic model of the tool (see Fig. 6), first, the position of the center of the wrist $\vec{p}_{WRC}$ relative to the RCM frame 0 is computed using the desired position $\vec{p}_{EE}$ and orientation R_{EE}:

$$\vec{p}_{WRC} = \begin{bmatrix} x \\ y \\ z \end{bmatrix} = \vec{p}_{EE} - \Big(l_{tip\_offset}\Big) R_{EE} \begin{bmatrix} 0 & 0 & 1 \end{bmatrix}^T \tag{4}$$

Subsequently, q_1 to q_3 are determined from the desired wrist center position $\vec{p}_{WRC}$ by employing a geometric solution:

$$\begin{bmatrix} q_1 \\ q_2 \\ q_3 \end{bmatrix} = \begin{bmatrix} \arcsin\Big(\frac{x}{\cos(q_2/q_3)}\Big) \\ \arcsin(-y/q_3) \\ \sqrt{x^2+y^2+z^2} \end{bmatrix} \tag{5}$$

The solutions for q_4, q_5 and q_6 are derived using the desired wrist orientation expressed by $R_{wrist} = R_{shaft}^{-1} R_{desired}$ and the analytical equation for R_{wrist}:

$$R_{wrist} = \begin{bmatrix} c_6 s_4 - c_4 c_5 s_6 & s_4 s_6 - c_4 c_5 c_6 & c_4 s_5 \\ c_4 c_6 - c_5 s_4 s_6 & -c_4 s_6 - c_5 c_6 s_4 & s_4 s_5 \\ s_5 s_6 & c_6 s_5 & c_5 \end{bmatrix} \tag{6}$$

$$R_{wrist} = \begin{bmatrix} r_{11} & r_{12} & r_{13} \\ r_{21} & r_{22} & r_{23} \\ r_{31} & r_{32} & r_{33} \end{bmatrix} \tag{7}$$

From Eq.(6), it is evident two solutions exist for the wrist bending angle q_5 given by the entry $r_{33} = c_5$. Next, evaluating the ratios of r_{23}/r_{13} and r_{31}/r_{32} yields equations for q_4 and q_6, respectively, for each bending angle solution. These equations can be solved to obtain the analytical inverse kinematics solutions for the degrees of freedom that control orientation:

$$\begin{bmatrix} q_4 \\ q_5 \\ q_6 \end{bmatrix}_1 = \begin{bmatrix} \arctan 2(r_{23}, r_{13}) \\ \arccos(r_{33}) \\ \arctan 2(r_{31}, r_{32}) \end{bmatrix} \tag{8}$$

$$\begin{bmatrix} q_4 \\ q_5 \\ q_6 \end{bmatrix}_2 = \begin{bmatrix} \arctan 2(-r_{23}, -r_{13}) \\ -\arccos(r_{33}) \\ \arctan 2(-r_{31}, -r_{32}) \end{bmatrix} \tag{9}$$

Given the unidirectional constraint on wrist bending, q_5 cannot be negative, and thus, only the first analytical solution for orientation, Eq. (8), is retained.

TABLE II: Modified Denavit-Hartenberg Parameters

i	Name	a_{i-1}	α_{i-1}	D_i	θ_i
1	PSM Yaw	0	$\pi/2$	0	$q_1 + \pi/2$
2	PSM Pitch	0	$-\pi/2$	0	$q_2 - \pi/2$
3	Insertion	0	$\pi/2$	$q_3 - l_{RCC}$	0
4	Wrist Outer Roll	0	0	$l_{shaft} + l_{wrist}/2$	q_4
5	Wrist Pitch	0	$-\pi/2$	0	q_5
6	Wrist Inner Roll	0	$\pi/2$	0	q_6
7	Virtual Tip Frame	0	0	l_{tip_offset}	0

C. Singularity Mitigation

The design for the RPR tool leads to the presence of a singularity when the wrist bending angle is zero ($q_5 = 0$). This is shown mathematically in Eq. (6). When $q_5 = 0$, there exists infinitely many solutions for the relation $q_4 + q_6 = \arctan 2(r_{22}, r_{21})$. When the wrist bending trajectory traverses the singularity, the axes of joints (q_4) and (q_6) coincide requiring the joint velocity of (q_4) to be momentarily infinite to maintain the desired trajectory which the robot physically cannot do. Typically, 3 main strategies can be adopted when the tool configuration passes close to singularity. Passing through the singularity and accepting any discontinuities in velocity is undesirable as it results in

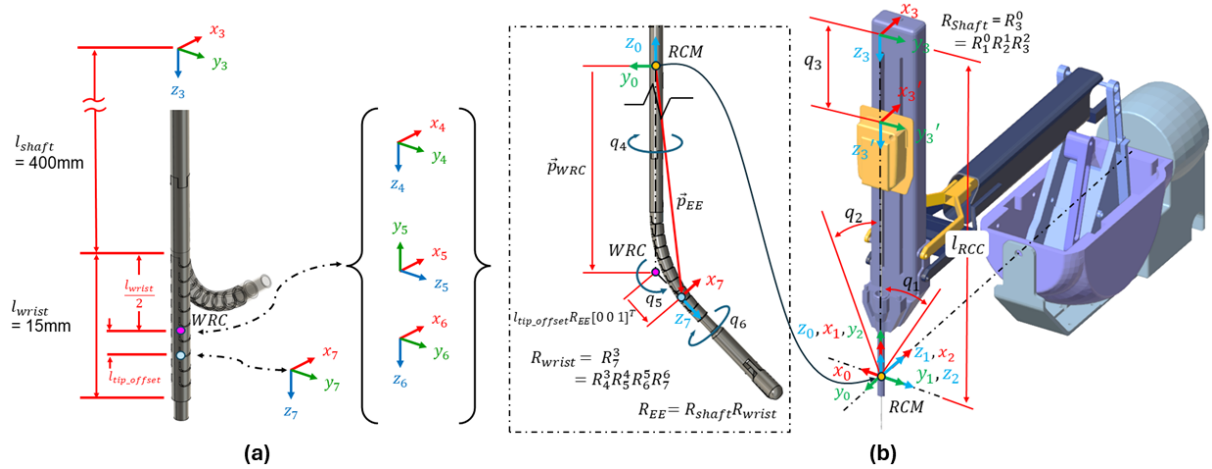

Fig. 6: RPR Tool Kinematics: a) Assignment of DH frames on the tool wrist. b) The decoupling of position and orientation where joints q_1 to q_3 control the position of the center of the wrist $\vec{p}_{WRC}$ and q_4 to q_6 control tool orientation. The PSM model is obtained from https://github.com/WPI-AIM/dvrk_env [18].

unpredictable movement which can be clinically dangerous and damaging for the robot. Avoiding trajectories that pass near the singularity is not viable since the surgeon may desire to work near the singularity. As a result, we adopt a mitigation strategy to inject small deviations in trajectories that pass nearby the wrist singularity. This is achieved by implementing a mapping in rotation space $R \in SO(3)$ that modifies the desired tool orientation, guiding the wrist to roll around the singularity as shown in Fig. 7a.

1) Singularity Identification: Proximity and the current wrist trajectory relative to the singularity are determined by monitoring the wrist bending angle q_5 and joint velocity $\dot{q}_5$. The singularity region is defined as a circle with $q_5 = 0$ as the center and a "radius" $\lambda = 5°$ representing the closest allowed proximity of q_5 to the singularity.

2) Rotation Direction: Shown in Fig. 6b, the rotation direction required to deviate around the singularity is determined by analyzing the change in orientation of the tool relative to the singularity. The rotation change from the singular configuration $R_{singular} = R_{wrist}(q_4 = 0, q_5 = 0, q_6 = 0)$ to the previous desired wrist orientation $R_{previous}$ is computed as $\Delta R_1 = (R_{singular})^T R_{previous}$. The rotation change from the previous to the current desired wrist orientation is given by $\Delta R_2 = (R_{previous})^T R_{wrist}$. These computed changes in rotation ΔR_1 and ΔR_2 are converted to axis-angle rotation vectors $\vec{u}_1$ and $\vec{u}_2$ respectively. The direction of rotation around the singularity corresponds to the direction of rotation between the projection of rotation vectors $\vec{u}_1$ and $\vec{u}_2$ on the shaft plane Π_{shaft} to ensure smooth and intuitive movement of the tool. The shaft plane normal, oriented along the z-axis of the tool shaft frame is given by $\vec{n}_{shaft} = R_{shaft}\begin{bmatrix}0 & 0 & 1\end{bmatrix}^T$. Lastly, the required direction of rotation is inferred from the angle ψ between the projected rotation vectors $\vec{u}_1$ and $\vec{u}_2$ on the shaft plane:

$$\psi = \arccos\left(\frac{\text{Proj}_{\Pi shaft}(\vec{u}_1) \cdot \text{Proj}_{\Pi_{shaft}}(\vec{u}_2)}{|\text{Proj}_{\Pi_{shaft}}(\vec{u}_1)||\text{Proj}_{\Pi_{shaft}}(\vec{u}_2)|}\right) \tag{10}$$

For the edge case where $\vec{u}_1$ and $\vec{u}_2$ are aligned, the rotation direction is resolved by examining the sign of $\vec{u}_2$'s x and y components. If both components are non-zero, the direction is inferred from the sign of their product. For rotations purely about the x or y axis, the direction is determined directly by the sign of $\vec{u}_2$'s corresponding rotational component.

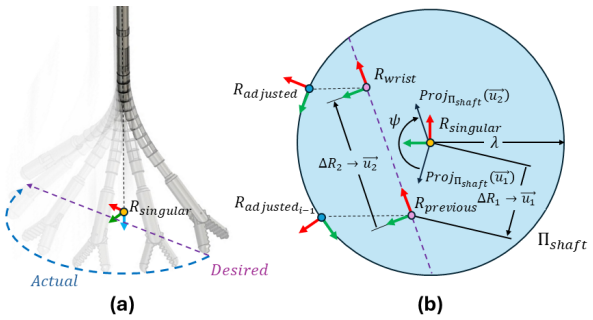

Fig. 7: Singularity mitigation. a) Visualization of the tool executing a wrist-rolling maneuver to navigate around the singularity. The wrist bending is exaggerated for clarity. b) Parameters of the singularity mitigation algorithm.

3) Orientation Adjustment: When the desired wrist orientation R_{wrist} enters the singularity region, a mapping function is applied which returns the necessary angle of rotation about the z axis γ to ensure the x axis of the end-effector frame is oriented in the radial direction from the center of the singular region. The function $\gamma = \mathbf{F}(q_5, \dot{q}_5, \psi)$ scales the magnitude of γ from $[0, 2\pi]$ according to the proximity of q_5 (derived from R_{wrist}) to the singular configuration and the direction of the bending trajectory (approaching or receding from $q_5 = 0$). The direction of the rotation is obtained directly from ψ, where a positive ψ corresponds to a counterclockwise rotation and vice-versa. Subsequently, R_{wrist} is modified by applying a z rotation by angle γ followed by a rotation about y by an angle of $\eta = \lambda = 5°$ to bend the wrist away from the singularity:

$$R_{adjusted} = R_{wrist} R_z(\gamma) R_y(\eta) \tag{11}$$

IV. TOOL CHARACTERIZATION

A. Wrist Tip Bending Accuracy

The accuracy of the PRB model was assessed by comparing its FK solutions against the measured tip trajectory of the wrist and the FK solutions obtained using a constant curvature model. The actual wrist tip trajectory was experimentally obtained by a 6 DoF electromagnetic(EM) tracker (Aurora, Northern Digital Inc.). The seed of the EM tracker was held in the grippers at a distance of 12mm from the end of the wrist (2mm in from the gripper tip). The positional PRB model FK solution was calculated using l_{tip_offset} = 19.5mm in consideration of the tracker position. The tip position FK solutions for the constant curvature model were obtained by geometric methods where the wrist and gripper is represented as a constant curvature arc with a length of 15mm and a straight length of 12mm extending tangentially from the end of the arc. The comparison can be seen in Fig. 8 over a bending range from 0° to 90°. The PRB model has a maximum positional error of 1.126mm occurring at a 90° wrist bending angle.

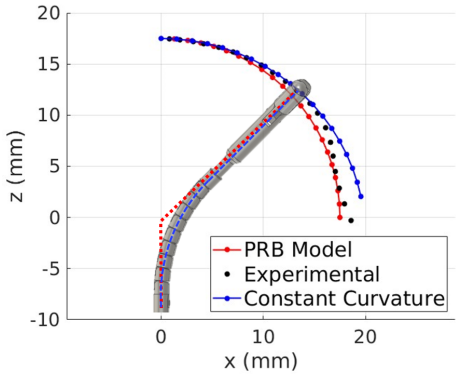

Fig. 8: Comparison between PRB model and Constant Curvature model FK tip position solutions against the measured gripper tip positions for 0° to 90° wrist bending. The visual representations for the geometric methods used by both the PRB model and Constant Curvature model to calculate their FK solutions are shown superimposed in red and blue respectively

B. Cable Tension versus Wrist Tip Bending Force

The mechanical efficiency of the wrist can be described by the relationship between tendon cable tension and the generated wrist tip force. A blocking force was applied on the wrist end by hanging known weights in opposition to the direction of wrist actuation. The test was repeated for fixed bending angles of 0°, 30°, and 60° with the weight incrementing by 50g from 0g to 200g. Tension in the tendon cable was measured using a load cell (LSB200, FUTEK Inc.) mounted on a linear positioning slider (460P Series, Newport Co.) to generate sufficient tension to maintain the wrist bending angle. The relationship between tendon cable tension and wrist tip force is seen in Fig. 9a. For a blocking force of 1.96N, 8N, 10N and 11N of tendon cable tension is required for 0°, 30°, and 60° of wrist bending angle respectively.

C. Lateral Blocking Force versus Lateral Deflection

The lateral stiffness of the overall wrist was described by its ability to resist perpendicular forces during bending. A deflecting force was applied at the tip of the wrist, perpendicular to the bending direction of the wrist, using microlinear positioning sliders (460P Series, Newport Co.). The lateral displacement was adjusted using the microlinear sliders, and the force was measured using a load cell (LSB200, FUTEK Inc.). The lateral force to lateral displacement relationship was obtained for wrist bending angles of 0°, 30°, and 60°, and is seen in Fig. 9b. The wrist was capable of exerting up to 1.5N of force laterally when experiencing 5mm of lateral deflection in a straight wrist configuration. The lateral force drops down to 0.8N for a 60° bending angle.

D. Concentric Tube Interactions

Due to friction effects between the inner and outer tubes of the wrist, a torsional lag occurs in the inner tube between its proximal and distal ends. To determine this relationship, the proximal end of the inner shaft was twisted from 0° to 140° back to 0°. The resultant roll angle of the inner tube at the distal end was measured using the EM tracker's pose. This was repeated for fixed bending angles of the outer shaft of 0°, 30°, 60°, and 90°. The difference in the roll angle between and the observed output roll angle can be seen in Fig. 9c for the various wrist bending angles. It can be seen that the inner shaft experienced little to no torsional lag at bending angles of 0° and 30° from the near one-to-one relationship between shaft input and output rotations. Slight lagging occurred at 60° wrist bending and significant lagging occurred for 90° wrist bending.

E. Wrist Curvature at Full Bending

The curvature of the wrist at full bending (90°) was verified by image processing software (ImageJ). The camera was aligned normal to the wrist's bending plane and an image was taken of the wrist against a reference background with a 12.7mm (1/2") grid. Characteristic points were defined along the bend of the wrist to fit a spline-curve. Measuring the spline, the average curvature is $107m^{-1}$ (9.35mm bending radius) and the midpoint curvature is $140m^{-1}$ (7.14mm bending radius)(Fig. 10a). These results are reasonable compared to the expected curvature of $125m^{-1}$ (8.00mm bending radius) given a constant curvature assumption (Fig. 10b).

V. TELEOPERATION SUTURING TESTING

Timed task studies were conducted on the suturing procedure. A suture pad (Soft Tissue Suture Pad, 3-Dmed) was used as the suturing medium. 4-0 sutures (Braided Coated Vicryl 13mm 3/8c reverse cutting needle, Ethicon Inc.) were used to execute simple interrupted sutures seen in Fig. 11. The suturing procedure was decomposed into three observable tasks: 1) Suture Needle Manipulation, 2) Suture Needle Puncture, and 3) Suture Knot Tying. Suture Needle Manipulation involves pickup of the suture needle, positioning the needle for puncturing into the target location and any manipulations of needle and thread that occur after

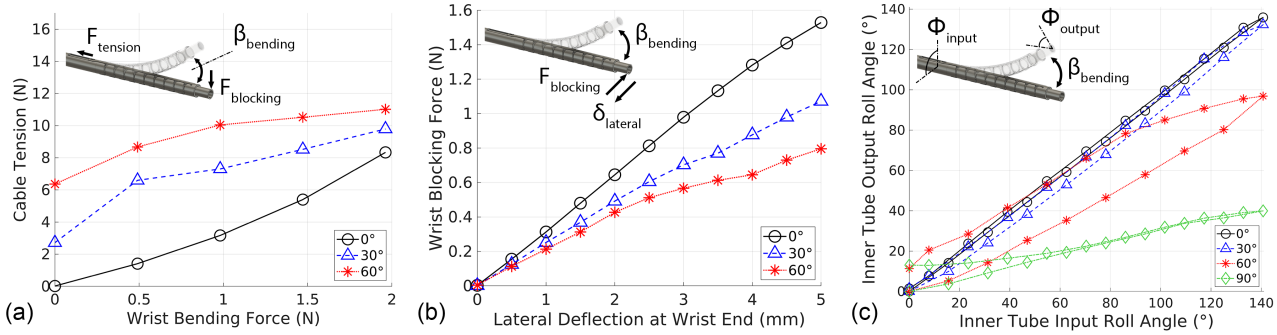

Fig. 9: a) Wrist bending force versus cable tension for wrist bending angles of 0°, 30°, and 60°. b) Lateral deflection at the wrist end versus lateral wrist blocking force. c) Input roll angle versus observed output roll angle for the inner shaft.

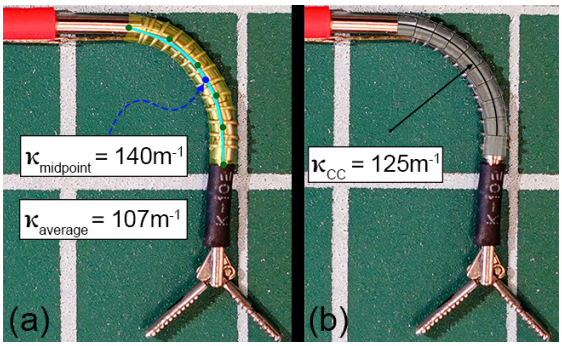

Fig. 10: Validated midpoint and average curvature in comparison to a constant curvature assumption for a 90° bending angle. a) The curvature is obtained from a spline-curve (cyan) fitted to characteristic points (green) obtained from an image mask (yellow). b) Simulated wrist bending under the constant curvature (κ_{CC}) assumption overlaid in grey.

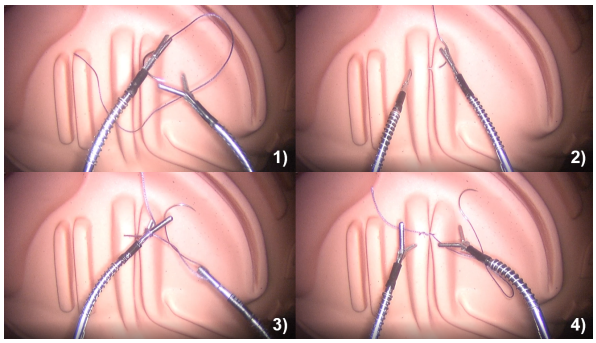

Fig. 11: Suturing procedure decomposed into three tasks: 1) Suture Needle Manipulation, 2) Suture Needle Puncture, 3) Suture Knot Tying. 4) Shows a completed Surgeon's Throw.

the completion of the puncturing and before the knot tying. Suture Needle Puncture involves driving the suture needle through both sides of the target location. Suture Knot Tying involves the wrapping and cinching of the thread to tie the Surgeon's Throw. To reduce setup and operator bias, the pick-up location of the suture needle and the target location of the suture was randomly varied to either be at the top, middle, or bottom of the lesion. The occurrence of user task errors such as a dropped needle or unintentional puncturing/damage of the suture pad were also recorded for each test.

The suturing task test was completed 10 independent times and the task completion timings for these tests are summarized in Table III. In all 10 tests, only one instance of a dropped needle was recorded as a task error.

TABLE III: Teleoperation Suturing Testing Task Timings

Task	Completion Time (min:sec)			
	Average	Std. Dev.	Max	Min
Suture Needle Manipulation $_{n=10}$	01:14	00:25	02:03	**00:35**
Suture Needle Puncture $_{n=10}$	01:30	00:33	02:48	**00:55**
Suture Knot Tying $_{n=10}$	02:00	00:39	03:14	**01:13**
Summary $_{n=10}$	04:43	-	08:05	**02:43**

VI. DISCUSSION

In the teleoperation testing we explicitly demonstrate that this wrist design is capable of suturing. The minimum completion times reflect that a single interrupted suture is achievable in under three minutes. Despite the significant variance in the task times observed, further training and testing would likely improve operator familiarity leading to a reduction in variance, average and minimum task times. The single instance of an observed task error suggests that kinematics of the PRB model is sufficiently accurate and intuitive for teleoperation control. The comparison of these timing results to other 2mm diameter tools [3] show significant reduction in average task time, variance and significant reduction in task errors. This comparison suggests that this tool design is significantly stronger, more reliable and more intuitive to operate. The results of the timed tests are significant considering that the suture pad is thicker and stiffer than the tissue found in OSB lesions and that the tool diameter is 1/4th the current daVinci 8mm instruments. Time is an important metric to consider in the performance of these tools as the operative times for OSB repair are long, averaging 223 minutes for current fetoscopic approaches [19].

The comparison of the tip position between the actual tool and the PRB kinematics from Fig. 8 show that the positional error increases as the wrist bending angle increases, with a maximum positional error of 1.126mm at a wrist angle of 90°. This increasing error is expected because the assumption

of the pseudo joint location at the midpoint of the wrist becomes less accurate at larger bending angles. Comparing the PRB model against the constant curvature model, it is observed that there is negligible difference in accuracy for small bending angles $\leq 30°$. The constant curvature model has better accuracy for bending angles between 30°-60° while the PRB model is more accurate for larger bending angles $\geq$60°.

Blocking force measurements were taken 2mm off the end of the wrist where the grippers connect onto the wrist end. This was done to ensure experiment repeatability and accuracy because of the difficulty in obtaining reliable measurements when fixturing on the grippers. The blocking forces at the wrist were measured until it became difficult to determine the wrist bend angle due to significant deformation. This implies that the maximum achievable blocking force of the wrist exceeds the 2N that has been validated as the data obtained does not capture failure. Taking the 2N value as the maximum force that can be exerted by the wrist, this is the strongest wrist that has been proposed in literature at the 2-3mm diameter scale that is capable of up to 90° of bending range. [20], [21], [22], [7], [8], [23], [3].

While this tool design borrow many design elements found from the works of Luo, Eastwood and Francis et. al. [6], [21], [7], [8], [22], the design of this tool possesses a unique combination of these features to enable superior wrist strength and stiffness while retaining the necessary range of motion for dexterous tasks. Further mechanical design optimizations can be made for additional strength. Refinement in tube cutting methods would enable the use smaller cutout geometries in the inner wrist tube which would lead to improved wrist strength under axial and torsional loading. Strength can also be improved using permanent attachment methods such as a weld joint between the grippers and the wrist. It is likely that suturing task times would reduce if the current off-the-shelf grippers were replaced with a purpose-built needle driver gripper such as those found in the work of Vandebroeck et al. [4].

The presented design has only been demonstrated for suturing. However, the construction of tools with scissors is necessary for the lesion dissection aspect of the repair and demonstrating the full repair procedure on silicone fetal and uterine models.

VII. CONCLUSION

In this work we present and demonstrate a novel 2mm diameter wrist design that is capable of producing the required dexterity, range of motion and force generation for suturing in the OSB procedure. This wrist design is able to achieve this with a significant decrease in tool diameter and with a more compact bending radius than what is currently presented in literature [4][3]. A PRB model has been implemented for the control of this tool with demonstrations of accuracy to the behavior of the actual tool over its entire articulation range. A protocol for singularity mitigation and avoidance has been implemented to improve teleoperation control intuition.

REFERENCES

[1] T. Looi, *et al.*, "A Simulation Study of Robotic In Utero Repair of Myelomeningocele," *Proc. Hamlyn Symp. Med. Robot.*, pp. 121–122, 2018.

[2] S. G. Petersen, *et al.*, "The Impact of Entry Technique and Access Diameter on Prelabour Rupture of Membranes Following Primary Fetoscopic Laser Treatment for Twin-twin Transfusion Syndrome," *Fetal Diagn. Ther.*, vol. 40, pp. 100–109, 2016.

[3] A. Law, *et al.*, "Feasibility of davinci-based 2mm tendon driven continuum tools for robotic repair of open spina bifida," *Proc. Hamlyn Symp. Med. Robot.*, pp. 107–108, 2024.

[4] T. Vandebroek, *et al.*, "Design and modelling of an anisotropic continuum robot end-effector for single-port access surgery suturing," *Advances in Mechanical Engineering*, vol. 15, no. 2, p. 16878132221140207, 2023.

[5] E. Amanov, *et al.*, "Transurethral anastomosis after transurethral radical prostatectomy: A phantom study on intraluminal suturing with concentric tube robots," *IEEE Transactions on Medical Robotics and Bionics*, vol. 2, no. 4, pp. 578–581, 2020.

[6] K. Ai Xin Jue Luo, *et al.*, "Design optimization for the stability of concentric tube robots," *IEEE Robotics and Automation Letters*, vol. PP, pp. 1–1, 08 2021.

[7] K. Eastwood, *et al.*, "Design of a contact-aided compliant notched-tube joint for surgical manipulation in confined workspaces," *Journal of Mechanisms and Robotics*, vol. 10, 10 2017.

[8] ——, "A steerable neuroendoscopic instrument using compliant contact-aided joints and monolithic articulation," *Journal of Medical Devices*, vol. 14, p. 025002, 06 2020.

[9] S. Robertson, *et al.*, "Mechanical fatigue and fracture of nitinol," *International Materials Reviews*, vol. 57, no. 1, pp. 1–37, 2012.

[10] E. Henderson, *et al.*, "On the experimental testing of fine nitinol wires for medical devices," *Journal of the mechanical behavior of biomedical materials*, vol. 4, no. 3, pp. 261–268, 2011.

[11] Z. Chen, *et al.*, "Software architecture of the da vinci research kit," in *2017 First IEEE International Conference on Robotic Computing (IRC)*. IEEE, 2017, pp. 180–187.

[12] R. Gondokaryono, *et al.*, "A Modular ROS-based dVRK Teleoperation Controller Architecture," *Proc. Hamlyn Symp. Med. Robot.*, pp. 139–140, 2022.

[13] K. Wen and J. Burgner-Kahrs, "Modeling and analysis of tendon-driven parallel continuum robots under constant curvature and pseudo-rigid-body assumptions," *Journal of Mechanisms and Robotics*, vol. 15, no. 4, p. 041003, 2023.

[14] R. J. Roesthuis and S. Misra, "Steering of multisegment continuum manipulators using rigid-link modeling and fbg-based shape sensing," *IEEE transactions on robotics*, vol. 32, no. 2, pp. 372–382, 2016.

[15] P. Rao, *et al.*, "How to model tendon-driven continuum robots and benchmark modelling performance," *Frontiers in Robotics and AI*, vol. 7, p. 630245, 2021.

[16] M. Pourafzal, *et al.*, "Piecewise constant strain kinematic model of externally loaded concentric tube robots," *Mechatronics*, vol. 74, p. 102502, 2021.

[17] S. H. Sadati, *et al.*, "Control space reduction and real-time accurate modeling of continuum manipulators using ritz and ritz–galerkin methods," *IEEE Robotics and Automation Letters*, vol. 3, no. 1, pp. 328–335, 2017.

[18] R. A. Gondokaryono and A. Agrawal, "An approach to modeling closed-loop kinematic chain mechanisms, applied to simulations of the da vinci surgical system," *Acta Polytechnica Hungarica*, vol. 16, no. 8, 2019.

[19] M. Belfort, *et al.*, "Fetoscopic Open Neural tube Defect Repair: Development and refinement of a Two-Port, Carbon Dioxide Insufflation Technique," *Obstetrics & Gynecology*, vol. 129, pp. 734–743, 2017.

[20] P. A. York, *et al.*, "A wrist for needle-sized surgical robots," in *2015 IEEE International Conference on Robotics and Automation (ICRA)*, 2015, pp. 1776–1781.

[21] K. Eastwood, *et al.*, "Kinetostatic Design of Asymmetric Notch Joints for Surgical Robots," in *IEEE/RSJ International Conference on Intelligent Robots and Systems*, 2016.

[22] P. Francis, *et al.*, "Miniaturized instruments for the da vinci research kit: Design and implementation of custom continuum tools," *IEEE Robotics and Automation Magazine*, vol. 24, no. 2, pp. 24–33, 2017.

[23] Y. Chitalia, *et al.*, "Modeling and control of a 2-dof meso-scale continuum robotic tool for pediatric neurosurgery," *IEEE Transactions on Robotics*, vol. 37, no. 2, pp. 520–531, 2021.